DOI: https://doi.org/10.14311/TPFM.2025.021

IMPROVING QCM BIOSENSOR EFFICIENCY BY FLOW CELL MODIFICATION

L. Kubíčková [1,2], O. Studeník [1,3], M. Plachá [3], M. Isoz [1,2]

[1] **Department of Mathematics, Informatics and Cybernetics, Faculty of Chemical Engineering, University of Chemistry and Technology, Technická 5, Prague 166 28, Czech Republic**

[2] **Czech Academy of Sciences, Institute of Thermomechanics, Dolejškova 5, Prague 182 00, Czech Republic**

[3] **Department of Chemical Engineering, Faculty of Chemical Engineering, University of Chemistry and Technology, Technická 5, Prague 166 28, Czech Republic**

Abstract

Biosensors based on quartz crystal microbalance (QCM) are often used for detection of biomolecules, pathogens, or viruses. The biological analyte gets captured at the QCM crystal surface, leading to a change in the crystal resonant frequency and analyte detection. However, with standard biosensor geometry, most of the analyte is captured in regions where the crystal sensitivity is limited. In this work, we investigate how changes in the biosensor geometry influence the spatial distribution of the captured analyte. Using a custom implementation of an immersed boundary method, we add obstacles on the non-detecting top wall of the biosensor flow cell, which is motivated by the possibility to 3D print this surface. Next, we simulate the biomolecules as Lagrangian particles with the Brownian motion taken into account and evaluate the probability of the analyte detection. Several different variants of obstacle shapes and layouts were tested. With the best obstacle configuration found, the amount of analyte captured in the most sensitive region of the crystal was 17% higher than in the standard configuration. The obtained results may be used (i) to generate QCM sensor geometries and validate this computational study, and (ii) as a basis for the development of less computationally demanding models usable in automatic optimization of the QCM biosensor geometry.

Keywords: CFD, lagrangian particle tracking, OpenFOAM, biosensor.

1 Introduction

Quartz Crystal Microbalance (QCM) technology is attractive for the medical, food, and environmental industry. Sensors based on QCM can be used for real-time measurements, including rapid detection or continuous monitoring [1]. The measured quantity is the QCM crystal resonant frequency because a change in the frequency signals a change in the mass that is adhered to the crystal surface. In biosensing applications, adhesion is ensured by biorecognition elements bonded to the crystal surface. The biorecognition elements include antibodies, enzymes, or molecularly imprinted polymers that allow for selective detection of, e.g., fungi, pathogenic microorganisms or viruses [2]. However, in the environment, these potentially harmful pathogens are usually present in low concentrations and there is a continuous effort to increase the efficiency of QCM biosensors [3].

The detection efficiency of the biosensor can be correlated with the amount of analyte captured near the center of the biosensor [2]. The reason is that standard QCM biosensors have a circular shape and the crystal mass sensitivity has a decreasing radial dependence. The maximum sensitivity is in the center of the biosensor and drops to almost zero near the edges [4]. Hence, the more analyte is captured near the center, the better the detection response is received.

The detection efficiency was shown to be influenced by changing the geometry of the biosensor flow cell. For example, decreasing the height of the flow cell has been reported to have a positive effect on the efficiency [2]. Nevertheless, up to the authors knowledge, there is no publication that presents usage of more complex optimization approaches as, e.g., topology optimization, to find the best geometry of the QCM biosensor flow cell.

In this contribution, we present an investigation designed to serve as an initial search for future topology optimization of the biosensor flow cell. We modify the flow cell geometry by adding obstacles onto the top, i.e., non-detecting, wall of the cell to obstruct and channel the flow.

For each modified geometry, the detection efficiency is evaluated by a computational model that includes two sequential steps. (i) First, we add obstacles to the top wall and model the flow inside the flow cell. This part is done using our custom immersed boundary method solver [5]. Applying the immersed boundary method, we can use the same computational mesh for all geometries. The effect of obstacles is accounted for by a scalar indicator field and adjustment of governing equations. (ii) Second, the resulting flow field is taken as an input into a Lagrangian particle tracking solver with the effect of the Brownian motion included [6]. Each tracked particle represents one pathogen and, when it touches a wall that represents the crystal surface, it is captured. Eventually, the detection efficiency is estimated as a ratio of the number of particles captured near the sensor center to the total number of particles.

2 Mathematical model

Immersed boundary method Let Ω be a finite volume (FV) computational mesh. To include obstacles using the immersed boundary method, the Ω is divided into three parts

$$\Omega = \Omega_\mathrm{f} \cup \Omega_\mathrm{sf} \cup \Omega_\mathrm{s} \tag{1}$$

where Ω_f contains FV cells that are fully submerged in fluid, Ω_sf comprises cells that are intersected by the solid-fluid interface and Ω_s contains cells fully inside the solid. This division is represented by an indicator field λ. In a cell $\Omega_P \in \Omega$, the λ field is defined as

$$\lambda = \begin{cases} 0 & \text{if } \Omega_P \in \Omega_\mathrm{f} \\ 1 & \text{if } \Omega_P \in \Omega_\mathrm{s} \\ \tilde{\lambda} \in (0,1) & \text{if } \Omega_P \in \Omega_\mathrm{sf} \end{cases}, \quad \tilde{\lambda} = 0.5\left[1 - \tanh\left(\frac{\sigma}{V^{\frac{1}{3}}}\right)\right] \tag{2}$$

where σ is the signed perpendicular distance from the cell center P to the surface and V is the cell volume.

The flow inside the biosensor is laminar and assumed to be described by Navier-Stokes equations in the form

$$\begin{gathered} \mathcal{M}(\boldsymbol{u}) = -\nabla\tilde{p} + \boldsymbol{f}_\mathrm{ib} \\ \nabla\cdot\boldsymbol{u} = 0 \end{gathered}, \qquad \begin{gathered} \mathcal{M}(\boldsymbol{u}) = \nabla\cdot(\boldsymbol{u}\otimes\boldsymbol{u}) - \nabla\cdot\left[\nu\left(\nabla\boldsymbol{u} + \nabla\boldsymbol{u}^\mathrm{T}\right)\right] \\ \boldsymbol{f}_\mathrm{ib} = \mathrm{ceil}(\lambda)\left(\mathcal{M}(\boldsymbol{u}_\mathrm{ib}) + \nabla\tilde{p}\right) \end{gathered} \tag{3}$$

where $\boldsymbol{u}$ is the velocity, $\tilde{p}$ the kinematic pressure and ν the kinematic viscosity. The effect of obstacles is accounted for by the source term $\boldsymbol{f}_\mathrm{ib}$, the scope of which is limited to cells with non-zero λ field by the ceil(λ) function. For the computation of $\boldsymbol{f}_\mathrm{ib}$, the pressure is taken from the previous iteration and $\boldsymbol{u}_\mathrm{ib}$ are prescribed velocity values. Inside obstacles, $\boldsymbol{u}_\mathrm{ib} = \boldsymbol{0}$, near the solid-fluid interface, $\boldsymbol{u}_\mathrm{ib}$ is calculated by polynomial interpolation between the values in the free stream and the boundary condition at the immersed boundary. For more details on the interpolation, see [7].

In addition to the immersed boundary, there are the inlet, outlet, and wall boundaries. At the immersed and wall boundary, the no-slip boundary condition for velocity and the zero-gradient condition for pressure are applied. At the inlet, the velocity is prescribed to satisfy a given flow rate, and the pressure is supplied by the zero-gradient condition. At the outlet, we prescribe the pressure directly and use a zero-gradient condition for the velocity.

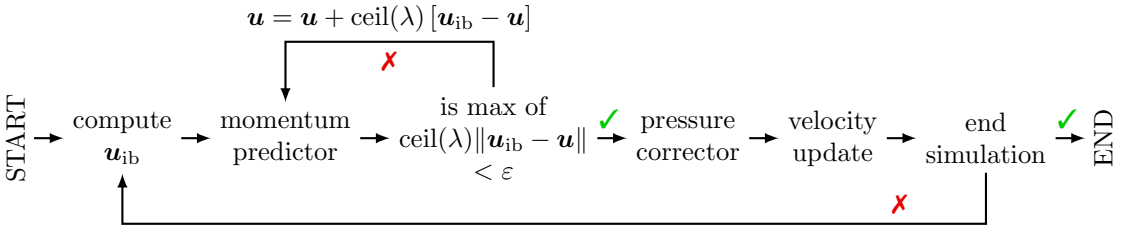

Figure 1: Modified loop of the SIMPLE algorithm where $\varepsilon = 10^{-8}$ is a predefined tolerance. Based on Kubíčková and Isoz [5].

symbol	parameter	value	unit
$\dot{Q}_{\text{inlet}}$	inlet flow rate	30	$\mu\text{m}\,\text{l}^{-1}$
p_{outlet}	outlet pressure	101.325	kPa
μ	fluid kinematic viscosity	10^{-6}	$\text{m}^2\,\text{s}^{-1}$
ρ	fluid density	998	$\text{kg}\,\text{m}^{-3}$
ρ_{P}	particle density	1335	$\text{kg}\,\text{m}^{-3}$
V_{P}	particle volume	60	nm^3
d_{P}	particle diameter	6	nm

Table 1: Model parameters.

Equations (3) complemented by the boundary conditions were discretized using the open source C++ library OpenFOAM [8]. A second-order upwind scheme was used to discretize the convection term in the momentum equation. A solution was acquired using the SIMPLE algorithm modified for the immersed boundary method, see Figure 1. The termination convergence criteria were set to 10^{-6} for all the fields.

Particles To model the movement and capture of biological particles, we used the model presented in Plachá et al. [6] for spherical, small, and sparsely distributed particles. Movement of each individual particle is modeled by Lagrangian tracking method and is described by Newtons second law of motion

$$\rho_{\text{P}}\, V_{\text{P}} \frac{\mathrm{d}\boldsymbol{u}_{\text{P}}}{\mathrm{d}t} = \boldsymbol{F}_{\text{D}} + \boldsymbol{F}_{\text{G}} + \boldsymbol{F}_{\text{B}}\,, \tag{4}$$

where ρ_{P} is the particle density, V_{P} the particle volume and $\boldsymbol{u}_{\text{P}}$ the particle velocity. On the right-hand side, $\boldsymbol{F}_{\text{D}}$ is the drag force, $\boldsymbol{F}_{\text{G}}$ the gravitation force, and $\boldsymbol{F}_{\text{B}}$ the Brownian force. Particle-particle interactions are neglected.

The computation of the drag force is based on the Stokes law and is implemented as

$$\boldsymbol{F}_{\text{D}} = 3\pi\mu\, d_{\text{P}}(\boldsymbol{u} - \boldsymbol{u}_{\text{P}})\,, \tag{5}$$

where d_{P} is the particle diameter and $\boldsymbol{u}$ the pre-calculated velocity of the fluid.

The Brownian force $\boldsymbol{F}_{\text{B}}$ was modeled utilizing a zero-mean independent Gaussian random numbers of unit variance $\boldsymbol{G} \in \mathbb{R}^3$ [9] as

$$\boldsymbol{F}_{\text{B}} = \rho_{\text{P}}\, V_{\text{P}}\, \boldsymbol{G} \sqrt{\frac{\pi S_0}{\Delta t_{\text{P}}}}, \quad S_0 = \frac{216\,\nu\, k_{\text{B}}\, T}{\pi^2\, \rho\, d_{\text{P}}^5 \left(\frac{\rho_{\text{P}}}{\rho}\right)^2}\,, \tag{6}$$

where ρ is the density of the fluid and Δt_{P} is the integration step.

Regarding the system boundaries, the particles enter via the inlet boundary with the same velocity as the fluid, and they exit via the outlet boundary. At the wall boundaries, two scenarios are distinguished. (i) The wall is the part of the flow cell itself, then the particles are rebound. (ii) The wall represents the crystal surface, then the particles get captured.

Biosensor efficiency To acquire representable statistical data, hundreds of thousands of particles are introduced into the biosensor and their movement is tracked. Afterwards, the biosensor efficiency η is calculated as

$$\eta = \frac{\text{particles captured in the most sensitive region}}{\text{escaped particles} + \text{all captured particles}}\,. \tag{7}$$

Model parameters All model parameters are listed in Table 1. The parameter values were set according to [2, 10].

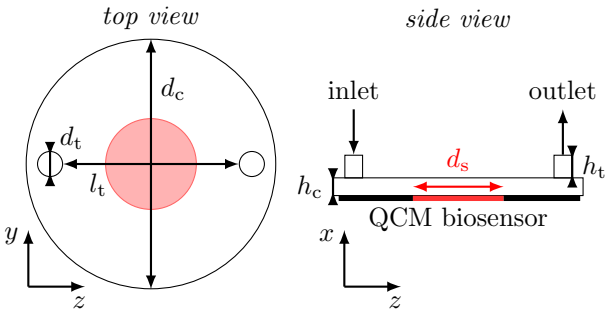

d_c	11 mm
d_t	0.5 mm
l_t	10 mm
h_c	0.1 mm
h_t	1 mm
d_s	2 mm

Figure 2: Flow cell geometry and dimensions. Red highlights the region of the crystal with the biggest sensitivity. Based on Scott Lynn Jr. et al. [2].

Flow cell geometry The geometry and dimensions of the studied flow cell are shown in Figure 2. The cell has a circular shape with one inlet and one outlet located near the edge. The crystal surface is on the bottom side of the flow cell and the most sensitive region of the biosensor is indicated in red, see Figure 2.

Mesh The corresponding computational mesh was created using the OpenFOAM blockMesh utility. Several different mesh resolutions were tested, with a focus on the quality of the flow field with a preset input flow rate (30 µl/min) and no obstacles present.

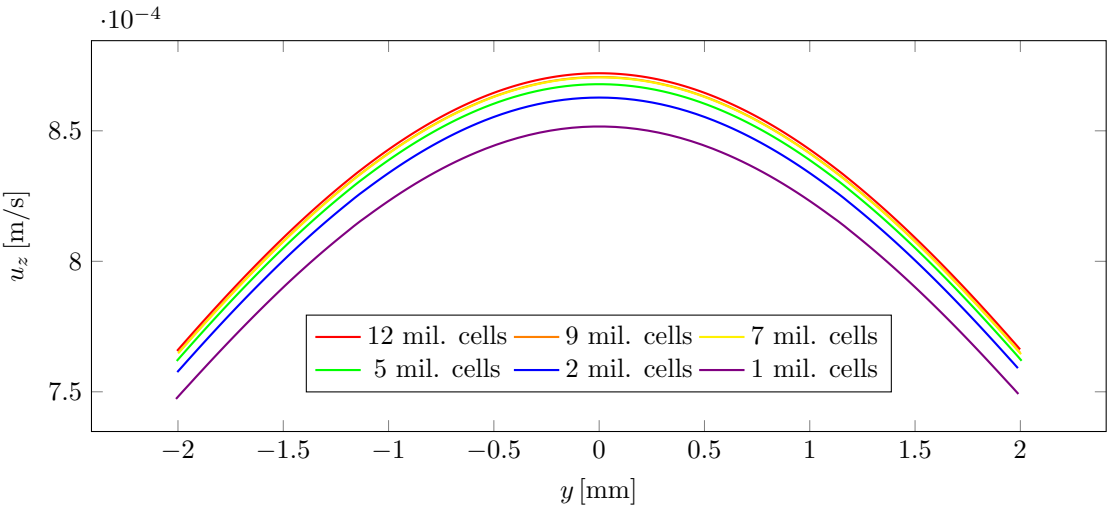

Figure 3: Comparison of u_z profiles across the most sensitive region for different mesh resolutions.

In particular, we compared the velocity profiles along the middle of the most sensitive region. The comparison is given in Figure 3. For meshes that have 5 and more million cells, the profile does not change significantly. However, the computational effort grows rapidly and, for further work, we chose the mesh with 5 million cells.

Obstacles geometry We considered two types of obstacles, spherical and sphero-cylindrical. A close-up view on the two types is given in Figure 4. Spherical obstacles were used to help redistribute and unify the flow. With more uniform flow, the particles would spend more time on average in the desired areas and would have a greater chance of being captured. Sphero-cylindrical obstacles were used to obstruct and channel the flow. In this way, more particles would go through the desired areas. However, the particles would travel at greater speed and have less time to get captured.

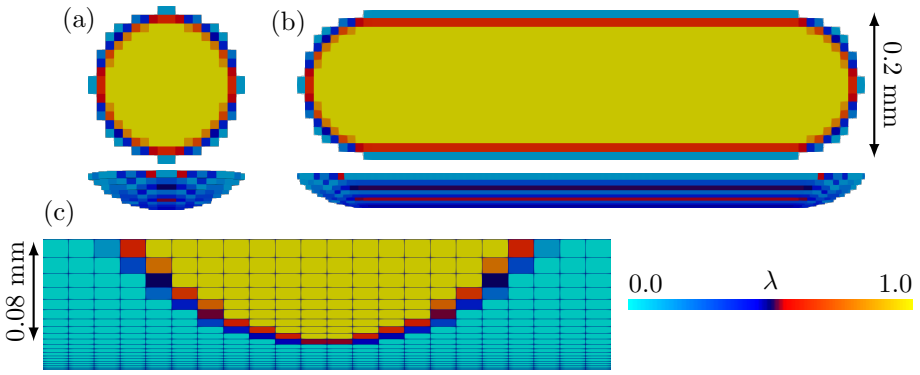

Figure 4: Visualization of obstacles, colored by λ field. (a) Top and side view of a spherical obstacle. (b) Top and side view of a sphero-cylindrical obstacle. (c) Zoom on the computational mesh around an obstacle.

3 Results

First, a referential simulation without obstacles was prepared to compute the default detection efficiency. The evolution of the efficiency η in the simulation is given in Figure 5. After introducing 200 thousand particles into the flow cell, the efficiency stabilized at the value of $\eta = 3.73\,\%$. In all subsequent simulations, the total number of introduced particles was kept at 200 thousand and they were introduced with a rate of 100 particles per second.

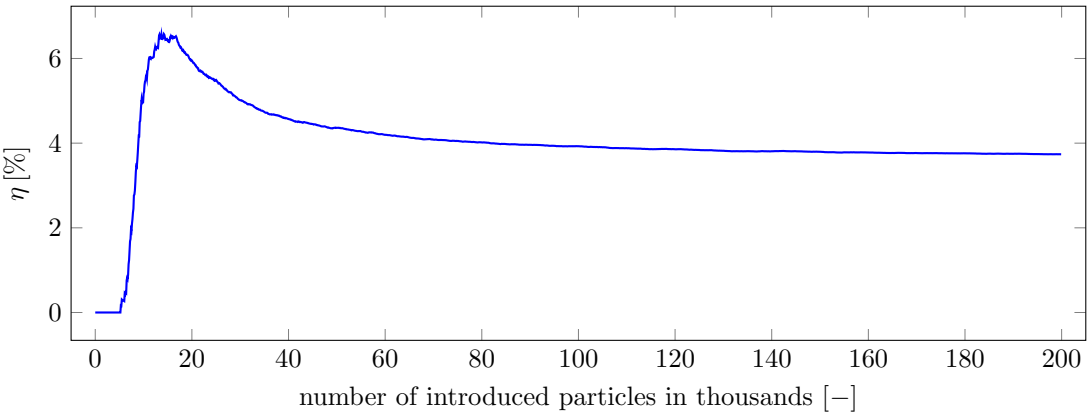

Figure 5: Evolution of the biosensor efficiency η with respect to the number of introduced particles.

Next, the effect of obstacles on efficiency was investigated. Several different layouts of obstacles were tested that incorporate one or both types of considered obstacle shapes.

In Figure 6, five chosen geometries having different obstacle layouts are compared with the geometry without obstacles. Geometries (b), (d) and (e) achieved a slightly higher efficiency by channeling the flow into the most sensitive region. Geometry (c) had the worst efficiency. Although the flow was more uniform when entering the most sensitive region, more particles got trapped outside of it.

The geometry with the best performance was geometry (f). The flow was channeled before and also after the most sensitive region. Such that, the particles could easily enter the region, but their way out was obstructed. In Figure 7, the qualitative results of the Lagrangian tracking simulation are compared for the geometry (f) and the default geometry (a). The improved detection efficiency was $\eta = 4.38\,\%$. Compared to the default efficiency, 17 % more particles were captured in the most sensitive region.

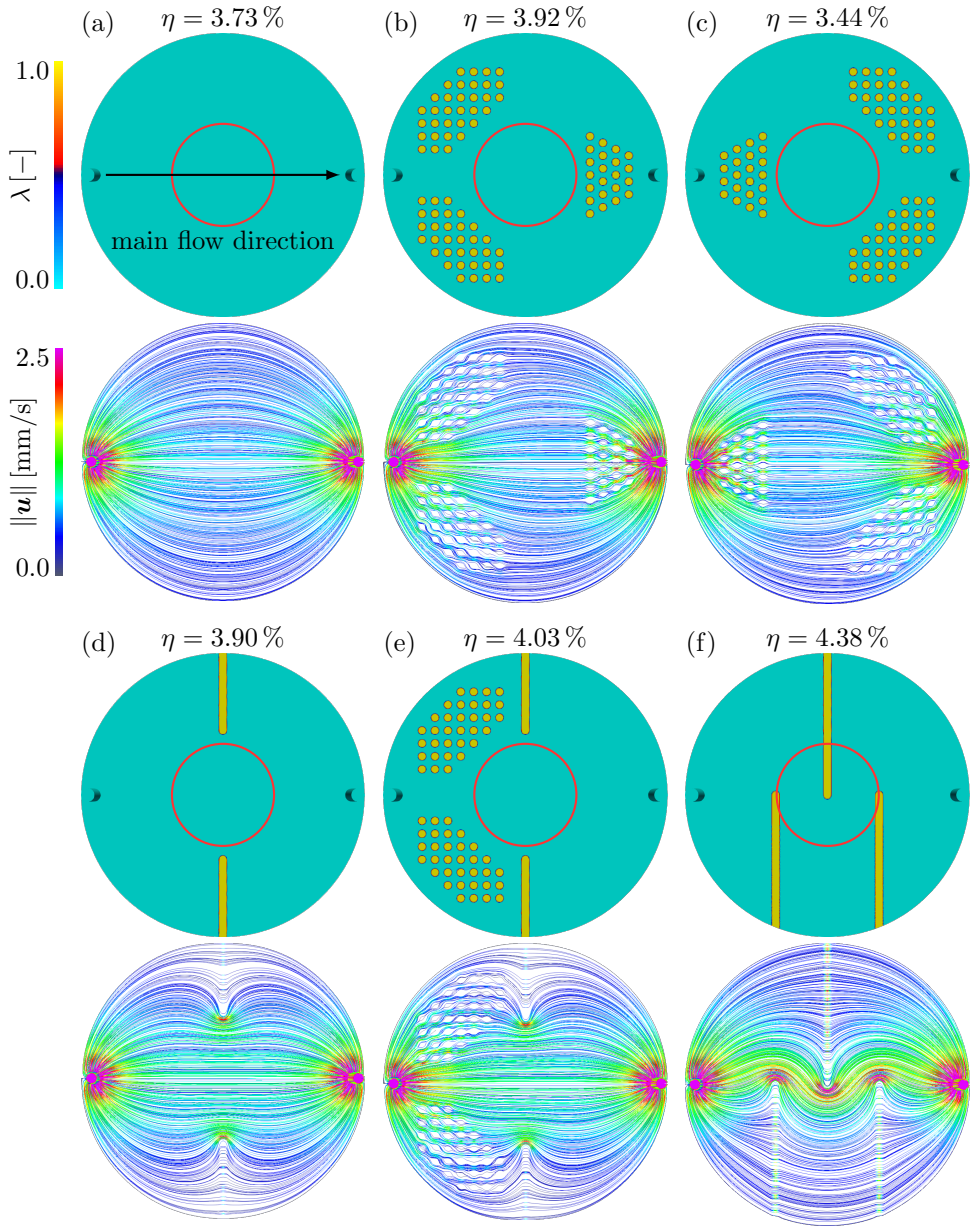

Figure 6: Biosensor geometries with different obstacle layouts and their corresponding η values. Each geometry is represented by the λ field at the top and stream lines at the bottom. Red circle indicates boundaries of the most sensitive region as given in Figure 2.

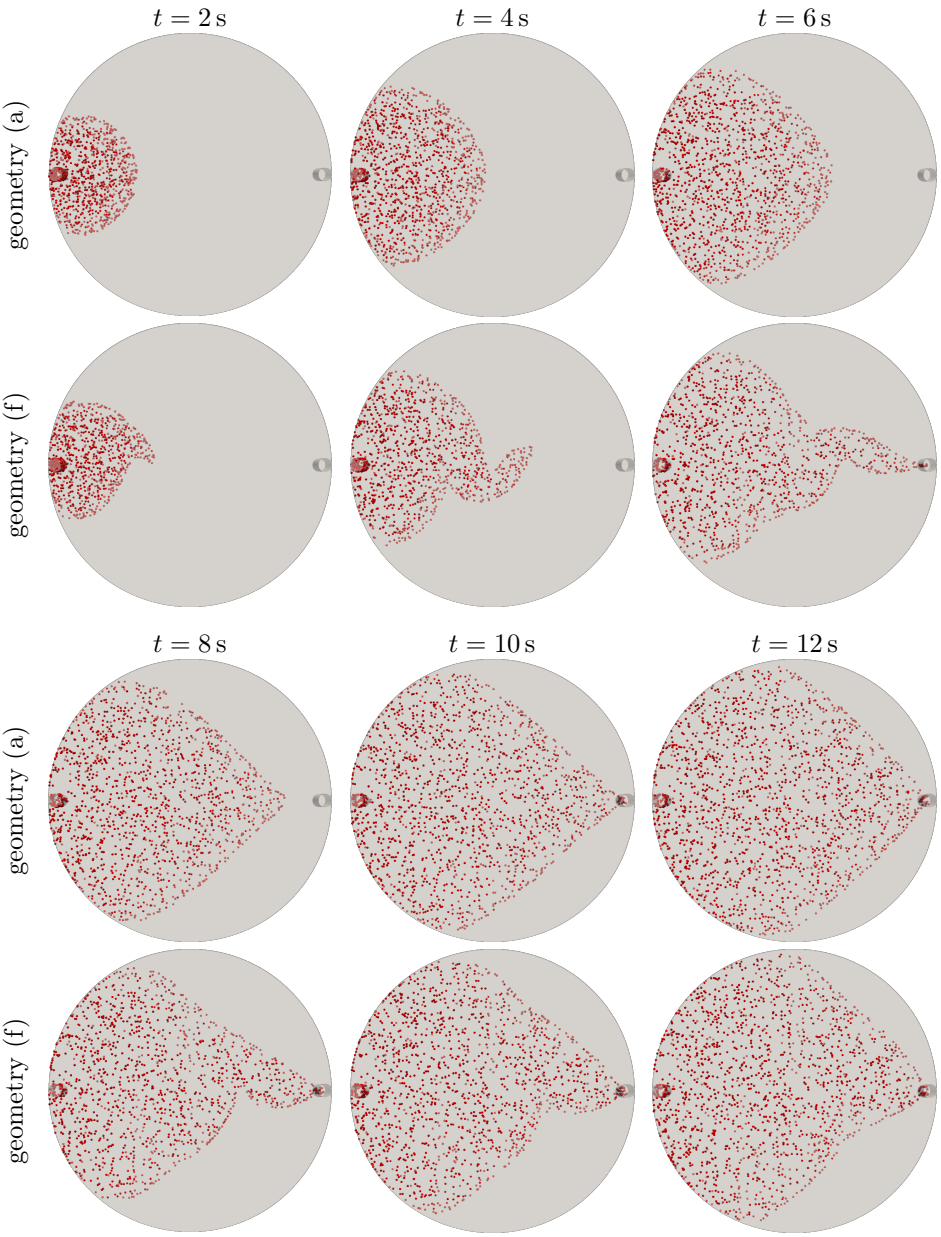

Figure 7: Temporal snapshots from the Lagrangian tracking simulation for geometries (a) and (f) as labeled in Figure 6. Particles are colored in red.

4 Conclusions

In this contribution, we investigated how changes in the flow cell geometry of a QCM biosensor affect its detection efficiency. To do so, a computational model capable of simulating the flow in the flow cell and the transport and capture of the detected analyte was prepared. Based on the model results, the detection efficiency was calculated as a ratio of the amount of analyte captured in the most sensitive region of the biosensor to the total amount of analyte. To test the influence of the flow cell geometry on the efficiency, the geometry was modified by adding obstacles onto its non-detecting top wall. Several different obstacle layouts were tested. An increase in efficiency was observed when the obstacles channeled the flow to the most sensitive region. The highest efficiency was achieved when the obstacles also obstructed the flow on its way out of the region. With the best geometry, the amount of analyte captured in the most sensitive region was 17 % higher than with the standard geometry. In future work, this study will serve as an initial search for a more complex topology optimization of the flow cell geometry.

Acknowledgment

The authors acknowledge the financial support provided by the Ministry of Education, Youth, and Sports of the Czech Republic via the project No. CZ.02.01.01/00/23_020/0008501 (METEX), co-funded by the European Union. This work was supported from the grant of Specific university research - grant No. A2 FCHI 2024 022. The work was financially supported by the institutional support RVO:61388998 and by the grant project with No. TN02000069/001N of the Technology Agency of the Czech Republic.

References

[1] Bonyadi, F., Kavruk, M., Ucak, S., Cetin, B., Bayramoglu, G., Dursun, A., Arica, Y. & Ozalp, V.: Real-time biosensing bacteria and virus with quartz crystal microbalance: Recent advances, opportunities, and challenges. *Critical Reviews in Analytical Chemistry*. vol. 54: (2023). pp. 2888–2899.

[2] Scott Lynn Jr., N., Forinová, M., Spasovová, M. & Vaisocherová-Lísalová, H.: Radial flow enhances QCM biosensor sensitivity. *Sensors and Actuators: B. Chemical*. vol. 401: (2024). page 134949. doi: 10.1016/j.snb.2023.134949.

[3] Lim, H., Saha, T., Tey, B., Tan, W. & Ooi, C.: Quartz crystal microbalance-based biosensors as rapid diagnostic devices for infectious diseases. *Biosensors and Bioelectronics*. vol. 168: (2020). page 112513.

[4] Cumpson, P. & Seah, M.: The quartz crystal microbalance; radial/polar dependence of mass sensitivity both on and off the electrodes. *Measurement Science and Technology*. vol. 1: (1990). page 544.

[5] Kubíčková, L. & Isoz, M.: On Reynolds-averaged turbulence modeling with immersed boundary method. In Šimurda, D. & Bodnár, T., editors, *Proceedings of Topical Problems of Fluid Mechanics 2023*: pp. 104–111. IT CAS: (02 2023).

[6] Plachá, M., Isoz, M., Kočí, P., Jones, M., Svoboda, M., Eastwood, D. & York, A.: Particle accumulation model in 3D reconstructed wall of a catalytic filter validated with time-resolved X-ray tomography. *Fuel*. vol. 356: (2024). page 129603.

[7] Isoz, M., Šourek, M. K., Studeník, O. & Kočí, P.: Hybrid fictitious domain-immersed boundary solver coupled with discrete element method for simulations of flows laden with arbitrarily-shaped particles. *Computers & Fluids*. vol. 244: (2022). page 105538.

[8] Weller, H., Greenshields, C. & et al., W. B. The OpenFOAM foundation: (2021).

[9] Li, A. & Ahmadi, G.: Computer simulation of deposition of aerosols in a turbulent channel flow with rough walls. *Aerosol Science and Technology*. vol. 18: (1993). pp. 11–24.

[10] Erickson, H.: Size and shape of protein molecules at the nanometer level determined by sedimentation, gel filtration, and electron microscopy. *Biological Procedures Online*. vol. 11: (2009). page 32.